

# Universal Fine-Grained Symmetry Inference and Enforcement for Rigorous Crystal Structure Prediction

Shi Yin<sup>†, \*</sup> Jinming Mu,<sup>2, \*</sup> Xudong Zhu,<sup>1</sup> and Linxin He<sup>†, 1</sup>

<sup>1</sup>*Institute of Artificial Intelligence, Hefei Comprehensive National Science Center, Hefei, Anhui, 230026, China*

<sup>2</sup>*Laboratory of Quantum Information, University of Science and Technology of China, Hefei, Anhui, 230026, China*

Crystal structure prediction (CSP), which aims to predict the three-dimensional atomic arrangement of a crystal from its composition, is central to materials discovery and mechanistic understanding. Existing deep learning models often treat crystallographic symmetry only as a soft heuristic or rely on space group and Wyckoff templates retrieved from known structures, which limits both physical fidelity and the ability to discover genuinely new material structures. In contrast to retrieval-based methods, our approach leverages large language models to encode chemical semantics and directly generate fine-grained Wyckoff patterns from composition, effectively circumventing the limitations inherent to database lookups. Crucially, we incorporate domain knowledge into the generative process through an efficient constrained-optimization search that rigorously enforces algebraic consistency between site multiplicities and atomic stoichiometry. By integrating this symmetry-consistent template into a diffusion backbone, our approach constrains the stochastic generative trajectory to a physically valid geometric manifold. This framework achieves state-of-the-art performance across stability, uniqueness, and novelty (SUN) benchmarks, alongside superior matching performance, thereby establishing a new paradigm for the rigorous exploration of targeted crystallographic space. This framework enables efficient expansion into previously uncharted materials space, eliminating reliance on existing databases or *a priori* structural knowledge.

Crystalline materials are fundamental to modern technologies spanning energy, electronics, medicine, and aerospace, and advancing these sectors relies on identifying novel crystal structures with tailored properties [1–5]. The vastness of the compositional and structural parameter space presents a fundamental bottleneck for materials discovery. Conventional pipelines, guided by chemical intuition and constrained by costly computations and experiments [6, 7], are intrinsically inefficient at exploring this space at scale. In recent years, artificial intelligence (AI), and deep learning-based generative models in particular, has emerged as a promising route to proposing candidate materials or predicting their properties at scale, demonstrating superior generalization capabilities and significant advantages in computational efficiency [8–15]. Within this landscape, the crystal structure prediction (CSP) task [8, 10, 13], which seeks the three-dimensional arrangement of atoms in the unit cell from a given composition, plays a pivotal role in AI-driven materials design workflows [11]. Diffusion models have become the dominant architecture for 3D structure generation [16, 17], and, for the CSP task, diffusion-based approaches also deliver state-of-the-art performance [10, 14].

However, the CSP task imposes particularly stringent requirements on the design of AI methods. Physically plausible crystal structures typically obey the symmetry constraints imposed by specific space groups. Learning and explicitly enforcing these symmetries can substantially reduce the search space of CSP, thereby improving both the efficiency and success rate of structure generation. Crystal symmetry strictly constrains the allowed Wyckoff positions, determining atomic multiplici-

ties, site symmetries, and the relative arrangement of atoms within the unit cell. Only when the given chemical composition is mathematically consistent with the corresponding Wyckoff positions can physically reasonable crystal structures be obtained.

However, existing AI methods only partially address this requirement. Some recent approaches on generating atomic structures condition the generator on a space group label [11, 14] but do not explicitly represent or enforce Wyckoff positions, so symmetry is only captured in a coarse global sense. Other works attempt to encode Wyckoff templates into a latent representation that modulates the generative process [12, 18], yet their modulation mechanisms do not guarantee that the final atomic coordinates satisfy the exact Wyckoff constraints. DiffCSP++ [10] goes further by enforcing strict space group symmetry defined by Wyckoff templates, but it assumes that a suitable space group and Wyckoff template are already known in the given lookup database. In practice, these templates are retrieved from existing structures via metric learning methods, such as CSPML [19]. However, restricting generation to retrieved templates confines the model to known symmetry patterns, thereby limiting its ability to discover genuinely new space-group and Wyckoff configurations for a given composition.

To address these fundamental limitations, we propose a symmetry-driven generative framework, which enables the *ab initio* generation of fine-grained Wyckoff site assignments directly from composition and atom counts, independent of any structural priors, as depicted in Fig. 1. Crucially, the predicted symmetries are imposed as hard geometric constraints to guide and modulate the diffusion process for three-dimensional crystal geometries,

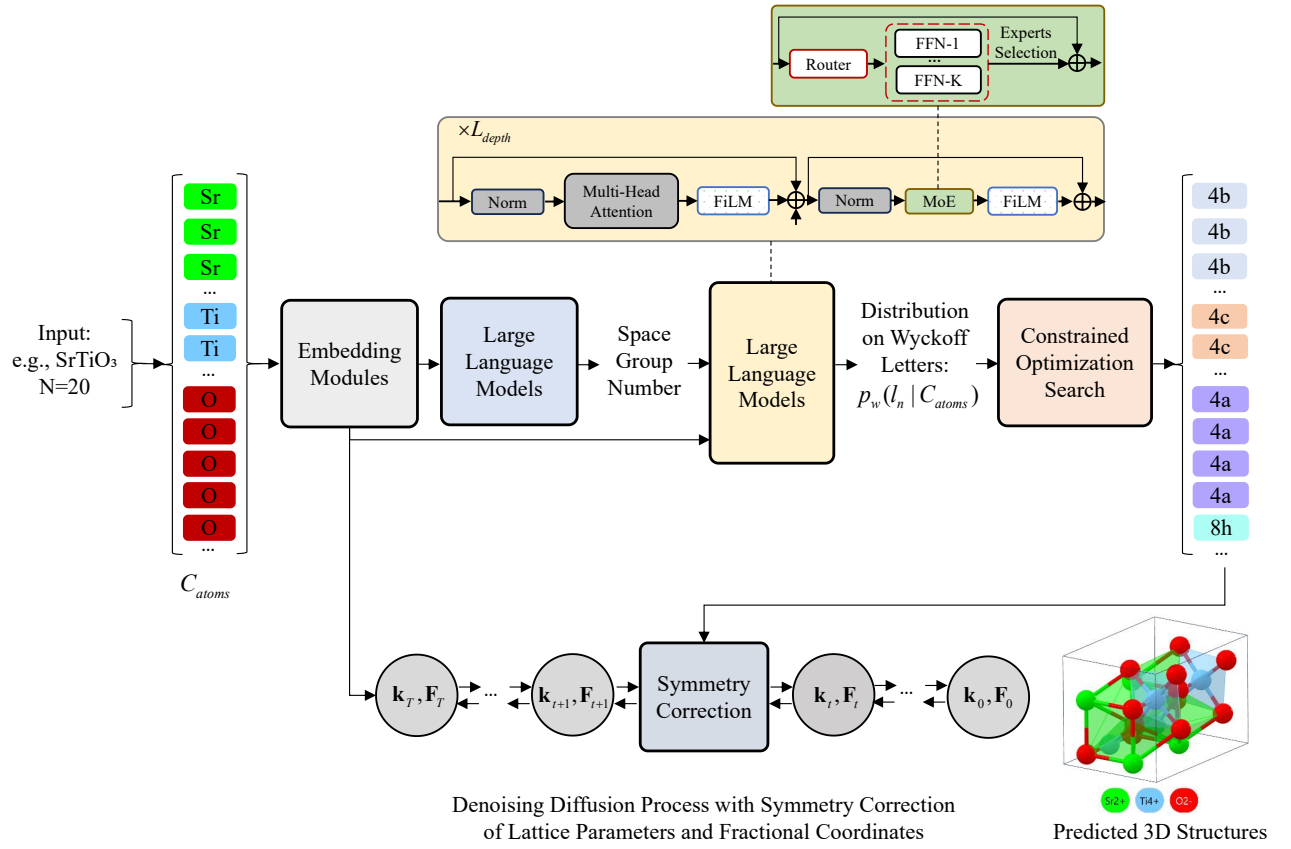


FIG. 1: Schematic of the proposed symmetry-driven generative framework.

thereby rectifying the denoising trajectory. By ensuring strict compliance with Wyckoff symmetry, our approach confines the generative process to a physically valid manifold, guaranteeing both structural plausibility and computational precision. As a result, this leads to a significant enhancement in the stability, uniqueness, and novelty (SUN) [14] of the discovered materials, as well as the matching rate metrics [20].

Below, we outline the core methodology, with full implementation details and training configurations provided in Supplementary Information A and B, respectively.

First, we use two large language models (LLMs) to directly infer fine-grained crystallographic symmetry from compositional inputs. Both models are built upon the Transformer architecture [21], and we replace the standard feed-forward networks within each Transformer block with soft mixture-of-experts (SoftMoE) layers [22] to enhance model capacity. This design enables multiple experts to specialize in distinct compositional patterns, substantially boosting model capacity without a commensurate rise in computational cost, as only a small, softly weighted subset of experts is activated at each position.

The first LLM, denoted as  $LLM_g$ , takes as input an

atomic sequence representation of the composition, expanded to explicitly reflect the atom counts  $N$  in the unit cell, and outputs a probability distribution over the 230 crystallographic space groups:

$$S_g = \arg \max_i p_g(i|C_{\text{atoms}}),$$

$$p_g(i|C_{\text{atoms}}) = LLM_g(C_{\text{atoms}}), \quad (1)$$

$$1 \leq i \leq 230,$$

where  $C_{\text{atoms}} = [A, A, A, \dots, B, B, B, B, \dots, C, C, \dots]$  is the expanded atomic sequence for elements  $A, B, C, \dots$  derived from the given composition, proportionally expanded to match the number of atoms in the unit cell;  $p_g[i]$  is the predicted probability that the crystal belongs to the  $i$ -th space group;  $S_g$  represents the predicted space group.

The second LLM, denoted as  $LLM_w$ , takes the same expanded atomic sequence together with the predicted space group  $S_g$  and outputs a probability distribution over Wyckoff letters compatible with that space group for each atom. Rather than concatenating  $S_g$  naively to the input, we encode the predicted space group into a continuous embedding and inject it into each transformer block via the feature-wise linear modulation (FiLM) [23] module. This FiLM-based conditioning ensures that Wyckoff predictions are explicitly modulated by the inferred

space group, rather than being learned in an implicitly entangled fashion. Concretely,  $\text{FiLM}(S_g)$  produces per-channel scaling and shifting coefficients that modulate the intermediate representations of  $LLM_w$ , allowing the model to adapt its representation to the predicted symmetry class:

$$p_w(l_n | C_{\text{atoms}}) = LLM_w(C_{\text{atoms}}, \text{FiLM}(S_g)), \quad (2)$$

$$l_n \in L(S_g), \quad 1 \leq n \leq N,$$

where  $p_w(l_n | C_{\text{atoms}})$  denotes the probability that the  $n$ -th atom is assigned to letter  $l$ ,  $L(S_g)$  is the set of admissible Wyckoff letters for space group  $S_g$ . Specific details regarding the network architectures and hyperparameter configurations of these two large language models are provided in Supplementary Information A.1-A.2 and B.1-B.2.

Second, we formulate the Wyckoff letter assignment for each atom as a constrained optimization problem based on the probability distribution  $p_w(l_n | C_{\text{atoms}})$  predicted by the LLM. This formulation strictly adheres to the combinatorial constraints imposed by the Wyckoff site multiplicity rules under the inferred space group symmetry. Specifically, the constrained maximization objective is defined as follows:

$$\{l_n^*\}_{n=1}^N = \arg \max_{\{l_n\}_{n=1}^N} \sum_{n=1}^N \log p_w(l_n | C_{\text{atoms}}),$$

$$\text{s.t. } l_n \in L(S_g),$$

$$\text{Count}_e(l_n) \bmod \text{mult}(l_n) = 0, \quad (3)$$

$$\sum_{l \in L(S_g)} \text{Count}_e(l) = N_e,$$

$$\forall e \in \mathcal{E} = \{A, B, C, \dots\},$$

where  $\text{mult}(l_n)$  refers to the multiplicity of Wyckoff letter  $l_n$ , and  $\text{Count}_e(l_n)$  is the number of atoms of element  $e$  assigned to  $l_n$ ,  $N_e$  is the number of atoms of element  $e$  in a cell, the set  $\{l_n^*\}_{n=1}^N$  represents the optimal Wyckoff letter assignment. The key point here is that  $\text{Count}_e(l_n)$  must be an integer multiple of  $\text{mult}(l_n)$ , a hard constraint that cannot be satisfied by simply using the maximum probability outputs of each token from the LLM. However, finding the solution for Eq. (3) via brute-force enumeration is computationally intractable, as the search space grows exponentially with the number of atoms, scaling as  $O(|L(S_g)|^N)$ . To overcome this bottleneck, we employ the constrained beam search algorithm to efficiently solve the optimization problem. By maintaining only the most promising candidates within a fixed beam width, this strategy drastically compresses the time complexity from exponential to a linear  $O(N)$ , rendering the prediction of physically valid Wyckoff assignments computationally tractable. Comprehensive details regarding this algorithm are provided in Supplementary Information A.3.

Third, we guide and constrain the diffusion-based generation of 3D atomic structures using the predicted space group and Wyckoff site template. To instantiate this approach, we adopt the graph neural network (GNN) applied by DiffCSP++[10] as the backbone network of diffusion model, effectively repurposing its exploration to strictly adhere to the symmetry constraints inferred by our method. Specifically, we employ a joint-rectification mechanism on both lattice and fractional coordinates. For the lattice, we constrain its  $O(3)$ -invariant logarithmic parameterization by applying a binary mask dictated by the inferred crystal family, ensuring the unit cell geometry strictly adheres to the specific constraints on lattice lengths and inter-axial angles defined by the crystal family. Simultaneously, for the fractional coordinates  $\mathbf{F}_t$ , we employ a subspace projection and reconstruction mechanism, effectively rectifying any symmetry violations in each denoising state of fractional coordinates, ensuring that the generated crystal structure strictly resides on the geometric manifold defined by the target Wyckoff symmetries. Further details regarding the lattice masking and coordinate reconstruction are available in Supplementary Information A.4.

To evaluate our approach, we benchmark it against a comprehensive suite of generative models. We adopt DiffCSP++ [10] as the primary baseline, as it represents the current state-of-the-art (SOTA) for standard CSP and serves as the most stringent benchmark for composition-conditioned structural generation, particularly for stability, uniqueness, and novelty (SUN) metrics. To provide a broader context for structural reconstruction fidelity, we also encompass CDVAE [24], DiffCSP [20], and CrystaLLM [9] in our comparative analysis, specifically regarding the Matching Rate metric. While MatterGen [14] is also a leading method in materials generation, it is excluded from direct comparison due to a fundamental discrepancy in task formulation. MatterGen employs a joint generation paradigm that co-samples chemical composition and structural coordinates. Although this enables unconstrained exploration, it lacks the strict conditionality inherent to CSP, where the core objective is to resolve the atomic structure for a fixed, pre-specified composition. Thus, a direct quantitative comparison is omitted

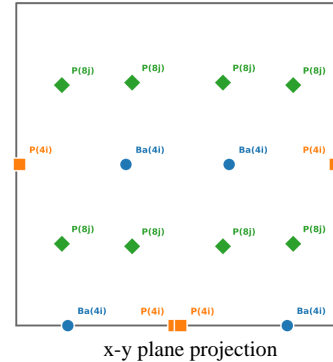
We adopt the SUN (Stability, Uniqueness, and Novelty) metrics [14] alongside the Top-20 Matching Rate [20] to provide a comprehensive evaluation of our model. The detailed definitions and calculation protocols for these metrics are provided in Supplementary Information C.1 and C.2. The SUN metrics emphasize physical plausibility, structural diversity, and originality, aspects that are more directly aligned with the objectives of open-ended discovery in materials science; while the Matching Rate prioritizes structural fidelity by quantifying the precision with which the model reconstructs the experimental ground-truth (GT) geometry within defined coordi-

Predicted Space Group: C2/m

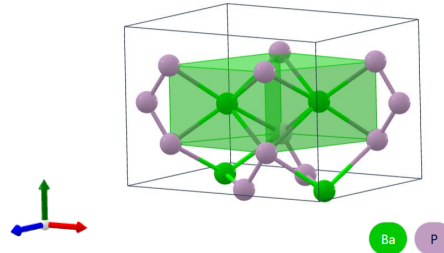
Predicted Wyckoff Template:

- **4i : Ba**  
 $(x_{\text{Ba}}, 0, z_{\text{Ba}}), (-x_{\text{Ba}}, 0, -z_{\text{Ba}})$   
 $(0.5+x_{\text{Ba}}, 1/2, z_{\text{Ba}}), (0.5-x_{\text{Ba}}, 1/2, -z_{\text{Ba}})$
- **4i : P**  
 $(x_{\text{P1}}, 0, z_{\text{P1}}), (-x_{\text{P1}}, 0, -z_{\text{P1}})$   
 $(0.5+x_{\text{P1}}, 1/2, z_{\text{P1}}), (0.5-x_{\text{P1}}, 1/2, -z_{\text{P1}})$
- ◆ **8j : P**  
 $(x_{\text{P2}}, y_{\text{P2}}, z_{\text{P2}}), (-x_{\text{P2}}, y_{\text{P2}}, -z_{\text{P2}})$   
 $(-x_{\text{P2}}, -y_{\text{P2}}, -z_{\text{P2}}), (x_{\text{P2}}, -y_{\text{P2}}, z_{\text{P2}})$   
 $(0.5+x_{\text{P2}}, 0.5+y_{\text{P2}}, z_{\text{P2}}), (0.5-x_{\text{P2}}, 0.5+y_{\text{P2}}, -z_{\text{P2}})$   
 $(0.5-x_{\text{P2}}, 0.5-y_{\text{P2}}, -z_{\text{P2}}), (0.5+x_{\text{P2}}, 0.5-y_{\text{P2}}, z_{\text{P2}})$

coordinate constraints



Predicted 3D structures:



Stable ✗  
 Novel ✗  
 Unique ✓

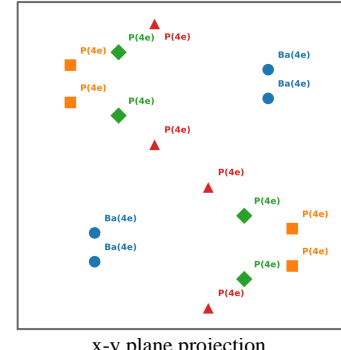
(a) Retrieved and Prediction results of DiffCSP++.

Predicted Space Group: P2<sub>1</sub>/C

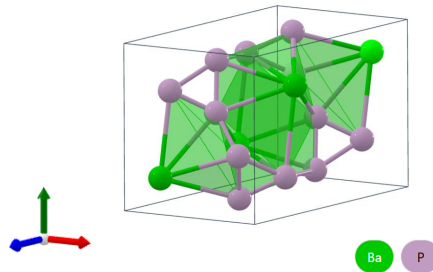
Predicted Wyckoff Template:

- **4e : Ba**  
 $(x_{\text{Ba}}, y_{\text{Ba}}, z_{\text{Ba}}), (-x_{\text{Ba}}, 0.5+y_{\text{Ba}}, 0.5-z_{\text{Ba}})$   
 $(-x_{\text{Ba}}, -y_{\text{Ba}}, -z_{\text{Ba}}), (x_{\text{Ba}}, 0.5-y_{\text{Ba}}, 0.5+z_{\text{Ba}})$
- **4e : P**  
 $(x_{\text{P1}}, y_{\text{P1}}, z_{\text{P1}}), (-x_{\text{P1}}, 0.5+y_{\text{P1}}, 0.5-z_{\text{P1}})$   
 $(-x_{\text{P1}}, -y_{\text{P1}}, -z_{\text{P1}}), (x_{\text{P1}}, 0.5-y_{\text{P1}}, 0.5+z_{\text{P1}})$
- ◆ **4e : P**  
 $(x_{\text{P2}}, y_{\text{P2}}, z_{\text{P2}}), (-x_{\text{P2}}, 0.5+y_{\text{P2}}, 0.5-z_{\text{P2}})$   
 $(-x_{\text{P2}}, -y_{\text{P2}}, -z_{\text{P2}}), (x_{\text{P2}}, 0.5-y_{\text{P2}}, 0.5+z_{\text{P2}})$
- ▲ **4e : P**  
 $(x_{\text{P3}}, y_{\text{P3}}, z_{\text{P3}}), (-x_{\text{P3}}, 0.5+y_{\text{P3}}, 0.5-z_{\text{P3}})$   
 $(-x_{\text{P3}}, -y_{\text{P3}}, -z_{\text{P3}}), (x_{\text{P3}}, 0.5-y_{\text{P3}}, 0.5+z_{\text{P3}})$

coordinate constraints



Predicted 3D structures:



Stable ✓  
 Novel ✓  
 Unique ✓

(b) Prediction results of our method.

FIG. 2: Visual comparison of prediction results from DiffCSP++ and our method for the target composition BaP<sub>3</sub> ( $N = 16$ ). The criteria for stability, uniqueness, and novelty follow the SUN metrics defined by Zeni et al.[14] and are detailed in Supplementary Information C.1.

TABLE I: Comparison of Top-20 SUN metrics (%) across three benchmarks. Results for DiffCSP++ [10] are reproduced using the official source code implementation [27], utilizing the CSPML [19] retrieval method to obtain space group templates as described in the original study.

Dataset	Method	Stability	Uniqueness	Novelty	SUN
MP-20	DiffCSP++	36.51	<b>100.0</b>	54.82	14.55
	Ours	<b>81.79</b>	<b>100.0</b>	<b>93.67</b>	<b>35.58</b>
Perov-5	DiffCSP++	75.77	<b>100.0</b>	99.52	73.39
	Ours	<b>94.98</b>	<b>100.0</b>	<b>99.67</b>	<b>92.42</b>
MPTS-52	DiffCSP++	11.95	<b>100.0</b>	45.97	5.44
	Ours	<b>42.43</b>	<b>100.0</b>	<b>70.53</b>	<b>25.94</b>

nate and symmetry tolerances. It is worth noting that, these two metrics can be inherently contradictory in a *Top-1* evaluation because a model must choose between replicating a known structure to achieve a high Matching Rate or exploring a previously unknown one to achieve high Novelty. This tension is effectively resolved in our *Top-20* setting. By generating multiple candidates for each composition, the model is afforded the capacity to simultaneously demonstrate structural fidelity by recovering the experimental ground truth and chemical creativity by proposing stable, novel phases. Thus, reporting both metrics at Top-20 provides a holistic assessment of the model’s dual role as both a precise structural reconstructor and a robust discovery engine for uncharted materials space.

All experiments are conducted on three standard CSP benchmark datasets: Perov-5 [25], MP-20 [26], and MPTS-52 [10]. These datasets were previously used in DiffCSP++ and are employed here with identical training, validation and testing splits to ensure a fair comparison. Detailed descriptions and statistical information regarding these three datasets are available in Supplementary Information C.2. The experimental results for the DiffCSP++ baseline are obtained using its official open-source scripts for standard training and inference [27]. Table I presents a side-by-side comparison between the performance of this original method and that of our symmetry-enhanced method.

As shown in Table I, our method yields notable and consistent improvements over DiffCSP++ across all three benchmarks on the comprehensive SUN metrics. On the MP-20 dataset, our method improves stability and novelty by approximately 124% and 71% respectively relative to the baseline. The advantages are even more pronounced on the challenging MPTS-52 dataset, where our method achieves a relative gain of about 255% in stability and 53% in novelty. Crucially, these component-level improvements compound to yield a striking 376% increase in the overall SUN metric. Even on Perov-5, which

TABLE II: Comparison of Top-20 Matching Rates (%) across three benchmarks. Experimental results for CDVAE [24], DiffCSP [20], and CrystaLLM [9] are taken from Antunes *et al.* [9]. Results for DiffCSP++ [10] are reproduced from the official source code [27] using the CSPML [19] retrieval-based template method as described in the original study.

Dataset	Method	Matching Rate
MP-20	CDVAE	66.95
	DiffCSP	77.93
	CrystaLLM	73.97
	DiffCSP++	74.65
	Ours	<b>81.70</b>
Perov-5	CDVAE	88.51
	DiffCSP	98.60
	CrystaLLM	97.60
	DiffCSP++	99.84
	Ours	<b>99.95</b>
MPTS-52	CDVAE	20.79
	DiffCSP	34.02
	CrystaLLM	33.75
	DiffCSP++	40.53
	Ours	<b>43.26</b>

features relatively simple structural motifs, our method maintains a clear advantage in stability while matching the saturated uniqueness and novelty scores of the baseline. The significant rise in the overall SUN metric across all benchmark datasets confirms that our method generates candidates that are simultaneously more physically stable and structurally novel, while preserving the high standards of uniqueness.

To tangibly demonstrate the advantage of our symmetry-driven approach over the retrieval-based baseline, we present a comparative case study for the target composition  $\text{BaP}_3$  ( $N = 16$ ) in Fig. 2. As illustrated in Fig. 2a, the DiffCSP++ baseline retrieves a Wyckoff template associated with Space Group 12 ( $C2/m$ ). This configuration assigns Ba atoms to a single  $4i$  site and P atoms to a mixed set of  $4i$  and  $8j$  sites. Such topological mismatch induces severe geometric frustration during structure generation, manifesting as prominent structural distortions with atomic clashes highlighted in red. Consequently, the generated structure is thermodynamically unstable and fails the novelty assessment.

In contrast, Fig. 2b demonstrates that our method successfully infers a symmetry-consistent Wyckoff template *ab initio* for the predicted space group (No. 14,  $P2_1/c$ ). It rigorously assigns atoms to four distinct  $4e$  Wyckoff orbits: one for Ba and three for P. By enforcing algebraic consistency, our approach generates a crystal structure fully aligned with the predicted symmetry, yielding a material candidate that satisfies all SUN metrics.

The performance disparity observed in Table I and Fig. 2 stems from the fundamental transition from retrieval-based memorization to generative reasoning. The baseline relies on CSPML, which essentially operates as a static lookup system. It rests on the isomorphism assumption, presupposing that for any new material, a structurally identical twin already exists in the training database. Consequently, this approach fails in data-sparse regimes or when exploring truly novel materials where no such prototype exists. When the model forces a novel composition into a retrieved but topologically mismatched template, it introduces geometric frustration. The atoms are coerced into energetically unfavorable coordination environments to satisfy incorrect symmetry constraints, directly leading to poor stability. This reliance on data lookup inherently confines the model to the known structural motifs, rendering it incapable of discovering new polymorphs that lie outside the existing library.

In stark contrast, our method reformulates symmetry determination as *ab initio* generative inference coupled with rigorous constrained optimization. Instead of memorizing and retrieving existing solutions, our model performs symmetry-aware reasoning to derive valid Wyckoff patterns for unseen compositions strictly from chemical rules. Crucially, a combinatorial optimization algorithm enforces algebraic consistency, ensuring the sum of site multiplicities matches the atomic stoichiometry. This mechanism empowers the model to explore uncharted chemical space while confining stochastic diffusion to a symmetry-compliant configurational space, guaranteeing output rationality. By eliminating symmetry-breaking artifacts of unconstrained generation, our framework enables inverse design of materials with high structural novelty and strict physical rigor.

Complementing the discovery-oriented SUN metrics, Table II presents the Top-20 Matching Rate, which quantifies the model’s ability to reconstruct experimentally known ground-truth structures. As shown, our method consistently achieves state-of-the-art performance across all three benchmarks, outperforming the DiffCSP++. While the numerical margin over the previous SOTA is incremental rather than dramatic, this result is scientifically significant when interpreted in the context of generative design. In *ab initio* materials discovery, the Matching Rate serves primarily as a validation metric rather than the ultimate objective; it confirms that the model’s generative distribution covers the manifold of physically realized structures. A high Matching Rate indicates that the symmetry constraints imposed by our framework do not overly restrict the search space or exclude valid ground-truth configurations. Instead, they effectively guide the diffusion process within a chemically reasonable manifold. Consequently, the combination of superior SUN scores (Table I) and leading Matching Rates (Table II) demonstrates that our method re-

solves the trade-off between exploration and exploitation: it is robust enough to recover known stable phases with high fidelity while possessing the generative flexibility to propose novel, stable polymorphs beyond the training distribution.

In summary, this work develops a symmetry-driven CSP framework that advances beyond conventional retrieval-based baselines. By reducing reliance on pre-existing prototypes, leveraging chemical rules, and enforcing strict algebraic consistency and symmetry compliance, it delivers robust performance in data-sparse regimes and novel material exploration. Experimental results show significant gains over state-of-the-art methods across comprehensive SUN metrics, transcending known structural motifs, as well as superior matching rates. This framework establishes a reliable, highly exploratory pathway for advanced functional material inverse design, redefining CSP from retrieval-based memorization to constrained *ab initio* generative inference.

This work was supported by the Advanced Materials–National Science and Technology Major Project (Grant No. 2025ZD0618401), the National Natural Science Foundation of China (Grant No. 12134012), the Strategic Priority Research Program of the Chinese Academy of Sciences (Grant No. XDB0500201). The numerical calculations were performed on the USTC High-Performance Computing facilities and Hefei advanced computing center.

---

\* Shi Yin and Jinming Mu contributed equally to this work. <sup>†</sup>Shi Yin (shiyin@iai.ustc.edu.cn) and Linxin He (helx@ustc.edu.cn) are the corresponding authors.

[1] M. A. Green, A. Ho-Baillie, and H. J. Snaith, The emergence of perovskite solar cells, *Nature photonics* **8**, 506 (2014).

[2] L. I. Berger, *Semiconductor materials* (CRC press, 2020).

[3] Q. Jiang and K. Zhu, Rapid advances enabling high-performance inverted perovskite solar cells, *Nature Reviews Materials* **9**, 399 (2024).

[4] J. Ding, D. Ji, Y. Yue, and M. M. Smedskjaer, Amorphous materials for lithium-ion and post-lithium-ion batteries, *Small* **20**, 2304270 (2024).

[5] R. Langer and D. A. Tirrell, Designing materials for biology and medicine, *Nature* **428**, 487 (2004).

[6] Z. W. Seh, J. Kibsgaard, C. F. Dickens, I. Chorkendorff, J. K. Nørskov, and T. F. Jaramillo, Combining theory and experiment in electrocatalysis: Insights into materials design, *Science* **355**, eaad4998 (2017).

[7] N. Marzari, A. Ferretti, and C. Wolverton, Electronic-structure methods for materials design, *Nature materials* **20**, 736 (2021).

[8] R. Jiao, W. Huang, P. Lin, J. Han, P. Chen, Y. Lu, and Y. Liu, Crystal structure prediction by joint equivariant diffusion on lattices and fractional coordinates, in *Workshops of the Eleventh International Conference on Learning Representations* (2023).

[9] L. M. Antunes, K. T. Butler, and R. Grau-Crespo, Crystal structure generation with autoregressive large language modeling, *Nature Communications* (2024).

[10] R. Jiao, W. Huang, Y. Liu, D. Zhao, and Y. Liu, Space group constrained crystal generation, in *The Twelfth International Conference on Learning Representations* (2024).

[11] S. Yang, S. Batzner, R. Gao, M. Aykol, A. Gaunt, B. McMorrow, D. Rezende, D. Schuurmans, I. Mordatch, and E. D. Cubuk, Generative hierarchical materials search, in *Advances in Neural Information Processing Systems* (2024) pp. 38799–38819.

[12] R. Zhu, W. Nong, S. Yamazaki, and K. Hippalgaonkar, Wyccrst: Wyckoff inorganic crystal generator framework, *Matter* **7**, 3469 (2024).

[13] Y. Han, C. Ding, J. Wang, H. Gao, J. Shi, S. Yu, Q. Jia, S. Pan, and J. Sun, Efficient crystal structure prediction based on the symmetry principle, *Nature Computational Science* (2025).

[14] C. Zeni, R. Pinsler, D. Züigner, A. Fowler, M. Horton, X. Fu, Z. Wang, A. Shysheya, J. Crabbé, S. Ueda, *et al.*, A generative model for inorganic materials design, *Nature* (2025).

[15] S. Yin, Z. Dai, X. Pan, and L. He, Advancing universal deep learning for electronic-structure hamiltonian prediction of materials, in *The Fourteenth International Conference on Learning Representations* (2026).

[16] J. Xu, X. Wang, W. Cheng, Y.-P. Cao, Y. Shan, X. Qie, and S. Gao, Dream3d: Zero-shot text-to-3d synthesis using 3d shape prior and text-to-image diffusion models, in *Proceedings of the IEEE/CVF Conference on Computer Vision and Pattern Recognition* (2023) pp. 20908–20918.

[17] C. Wang, H.-Y. Peng, Y.-T. Liu, J. Gu, and S.-M. Hu, Diffusion models for 3d generation: A survey, *Computational Visual Media* **11**, 1 (2025).

[18] Z. Cao, X. Luo, J. Lv, and L. Wang, Space group informed transformer for crystalline materials generation, *Science Bulletin* (2025).

[19] M. Kusaba, C. Liu, and R. Yoshida, Crystal structure prediction with machine learning-based element substitution, *Computational Materials Science* **211**, 111496 (2022).

[20] R. Jiao, W. Huang, P. Lin, J. Han, P. Chen, Y. Lu, and Y. Liu, Crystal structure prediction by joint equivariant diffusion, in *Advances in Neural Information Processing Systems 36: Annual Conference on Neural Information Processing Systems 2023* (2023).

[21] A. Vaswani, N. Shazeer, N. Parmar, J. Uszkoreit, L. Jones, A. N. Gomez, L. Kaiser, and I. Polosukhin, Attention is all you need, in *Conference on Neural Information Processing Systems* (2017) pp. 5998–6008.

[22] J. Puigcerver, C. R. Ruiz, B. Mustafa, and N. Houlsby, From sparse to soft mixtures of experts, in *The Twelfth International Conference on Learning Representations* (2024).

[23] E. Perez, F. Strub, H. De Vries, V. Dumoulin, and A. Courville, Film: Visual reasoning with a general conditioning layer, in *Proceedings of the AAAI conference on artificial intelligence* (2018).

[24] T. Xie, X. Fu, O. Ganea, R. Barzilay, and T. S. Jaakkola, Crystal diffusion variational autoencoder for periodic material generation, in *The Tenth International Conference on Learning Representations* (2022).

[25] I. E. Castelli, D. D. Landis, K. S. Thygesen, S. Dahl, I. Chorkendorff, T. F. Jaramillo, and K. W. Jacobsen, New cubic perovskites for one-and two-photon water splitting using the computational materials repository, *Energy & Environmental Science* **5**, 9034 (2012).

[26] A. Jain, S. P. Ong, G. Hautier, W. Chen, W. D. Richards, S. Dacek, S. Cholia, D. Gunter, D. Skinner, G. Ceder, *et al.*, Commentary: The materials project: A materials genome approach to accelerating materials innovation, *APL materials* **1**, 011002 (2013).

[27] <https://github.com/jiaor17/DiffCSP-PP>.

[28] J. Su, M. H. M. Ahmed, Y. Lu, S. Pan, W. Bo, and Y. Liu, Roformer: Enhanced transformer with rotary position embedding, *Neurocomputing* **568**, 127063 (2024).

[29] H. Yang, C. Hu, Y. Zhou, X. Liu, Y. Shi, J. Li, G. Li, Z. Chen, S. Chen, C. Zeni, *et al.*, Mattersim: A deep learning atomistic model across elements, temperatures and pressures, *arXiv preprint arXiv:2405.04967* (2024).

[30] S. P. Ong, W. D. Richards, A. Jain, G. Hautier, M. Kocher, S. Cholia, D. Gunter, V. L. Chevrier, K. A. Persson, and G. Ceder, Python materials genomics (pymatgen): A robust, open-source python library for materials analysis, *Computational Materials Science* **68**, 314 (2013).

[31] J. Schmidt, N. Hoffmann, H.-C. Wang, P. Borlido, P. J. Carriço, T. F. Cerqueira, S. Botti, and M. A. Marques, Large-scale machine-learning-assisted exploration of the whole materials space, *arXiv preprint arXiv:2210.00579* (2022).

## Appendix A: Detailed Design on Model Architectures and Algorithms

### A.1. Input Featurization and Embeddings

As defined in the main text, the input to our language models is the expanded atomic sequence  $C_{\text{atoms}}$ . For the  $n$ -th atom in this sequence (where  $1 \leq n \leq N$ ), let  $v_n$  denote its corresponding token index in the vocabulary. To capture the rich chemical semantics required for crystallographic reasoning, we construct a composite input representation  $\mathbf{x}_n$  by fusing the learnable token embedding with explicit physicochemical features derived from the periodic table.

**Token Embeddings.** We utilize a learnable lookup table  $\mathbf{E}_{\text{tok}} \in \mathbb{R}^{V \times D}$  to map the discrete index  $v_n$  of each semantic token (e.g. the element type) to a dense semantic vector  $\mathbf{h}_n$ :

$$\mathbf{h}_n = \mathbf{E}_{\text{tok}}[v_n] \in \mathbb{R}^D. \quad (\text{A1})$$

**Physicochemical Features.** Simultaneously, for the  $n$ -th atom, we retrieve its explicit chemical attributes: the atomic number  $Z_n$ , the group number  $G_n$ , and the period number  $P_n$ . To effectively integrate this discrete information, we employ three separate embedding layers ( $\mathbf{E}_Z, \mathbf{E}_G, \mathbf{E}_P$ ) to project these attributes into the latent space. The projected features are concatenated and fused via a multi-layer perceptron (MLP) to form the chemical feature vector  $\mathbf{f}_n \in \mathbb{R}^D$ :

$$\mathbf{f}_n = \text{MLP}(\mathbf{E}_Z[Z_n] \oplus \mathbf{E}_G[G_n] \oplus \mathbf{E}_P[P_n]), \quad (\text{A2})$$

where  $\oplus$  denotes the concatenation operation.

**Final Input Representation.** The final input embedding  $\mathbf{x}_n$  passed to the first transformer layer is the element-wise sum of the token embedding and the chemical feature vector, ensuring that both identity and periodicity information are preserved:

$$\mathbf{x}_n = \mathbf{h}_n + \mathbf{f}_n. \quad (\text{A3})$$

**Symmetry Conditioning.** For the symmetry-conditioned model  $LLM_w$ , the space group label  $S_g$  predicted by  $LLM_g$  is explicitly embedded to serve as the global context. We use a dedicated embedding layer  $\mathbf{E}_{sg}$  to map  $S_g$  to a continuous vector  $\mathbf{e}_{sg}$ :

$$\mathbf{e}_{sg} = \mathbf{E}_{sg}[S_g] \in \mathbb{R}^D. \quad (\text{A4})$$

This vector  $\mathbf{e}_{sg}$  is subsequently used to generate the modulation parameters for the FiLM layers in the Transformer blocks.

### A.2. Transformer Block with SoftMoE and FiLM

Both  $LLM_g$  and  $LLM_w$  rely on a unified modified Transformer architecture. To handle the complex mapping between composition and symmetry, we replace the standard Feed-Forward Network (FFN) with Soft Mixture-of-Experts (SoftMoE) layers in both models to enhance capacity without increasing inference cost. In the following formulation, we detail the architecture of the more complex  $LLM_w$ , which explicitly incorporates symmetry conditioning. It is important to note that  $LLM_g$  shares a similar structural backbone, including the Multi-head attention module and the SoftMoE mechanism, but omits the Feature-wise Linear Modulation (FiLM) modules, as it operates without prior symmetry conditions.

**Multi-Head Attention with RoPE and FiLM.** Let  $\mathbf{X}$  be the input to the attention block. We first apply LayerNorm to obtain  $\mathbf{Y} = \text{LayerNorm}(\mathbf{X})$ . To implement multi-head attention with  $H$  heads, the input is projected into  $H$  distinct subspaces. For each head  $h \in \{1, \dots, H\}$ , the Queries, Keys, and Values are computed as:

$$\mathbf{Q}_h = \mathbf{W}_Q^h \cdot \mathbf{Y}, \quad \mathbf{K}_h = \mathbf{W}_K^h \cdot \mathbf{Y}, \quad \mathbf{V}_h = \mathbf{W}_V^h \cdot \mathbf{Y}. \quad (\text{A5})$$

Rotary Positional Embeddings (RoPE) [28] are applied to each  $\mathbf{Q}_h$  and  $\mathbf{K}_h$  to encode relative positions. The attention output for the  $h$ -th head, denoted as  $\mathbf{A}_h$ , is computed via softmax, and the final output  $\mathbf{O}$  is obtained by concatenating all heads and applying a linear projection:

$$\begin{aligned} \mathbf{A}_h &= \text{softmax}\left(\frac{\mathbf{Q}_h \cdot \mathbf{K}_h^\top}{\sqrt{d_k}}\right) \cdot \mathbf{V}_h, \\ \mathbf{O} &= \text{Concat}(\mathbf{A}_1, \dots, \mathbf{A}_H) \cdot \mathbf{W}_O. \end{aligned} \quad (\text{A6})$$

In  $LLM_w$ , this output is modulated by the space group embedding  $\mathbf{e}_{sg}$  via Feature-wise Linear Modulation (FiLM). The modulation parameters  $(\gamma, \beta)$  are derived from  $\mathbf{e}_{sg}$ :

$$(\gamma, \beta) = \text{MLP}(\mathbf{e}_{sg}), \quad \text{FiLM}(\mathbf{O}) = \mathbf{O} \odot (1 + \gamma) + \beta, \quad (\text{A7})$$

where  $\cdot$  denotes matrix multiplication and  $\odot$  denotes element-wise multiplication.

**SoftMoE Layer with FiLM.** The intermediate representation is passed to the SoftMoE layer. Let  $\mathbf{Y}$  denote the normalized input to this block. We compute the expert dispatch weights by mapping the input to expert scores  $\mathbf{W}_r \mathbf{Y}$ . For each token  $n$ , we select the top- $k$  experts  $T_n$ . The routing weights  $g_{n,e}$  for the  $e$ -th expert and  $n$ -th token are normalized within the selected set:

$$\begin{aligned} \mathbf{P} &= \text{softmax}(\mathbf{W}_r \mathbf{Y}), \\ g_{n,e} &= \frac{P_{n,e}}{\sum_{j \in T_n} P_{n,j}} \cdot \mathbb{I}[e \in T_n]. \end{aligned} \quad (\text{A8})$$

Here,  $\mathbb{I}[e \in T_n]$  denotes the indicator function, taking value 1 if expert  $e$  is in  $T_n$ , and 0 otherwise.

The output  $\mathbf{Y}_{out}$  aggregates the processed features from all experts:

$$\mathbf{Y}_{out} = \sum_{e=1}^E \text{Scatter}(n, g_{n,e} \cdot \text{FFN}_e(\mathbf{Y}_n)). \quad (\text{A9})$$

Similar to the attention block, the output of the SoftMoE layer in  $LLM_w$  is modulated by the space group context:

$$\begin{aligned} (\gamma', \beta') &= \text{MLP}(\mathbf{e}_{sg}), \\ \text{FiLM}(\mathbf{Y}_{out}) &= \mathbf{Y}_{out} \odot (1 + \gamma') + \beta'. \end{aligned} \quad (\text{A10})$$

### A.3. Constrained Beam Search Algorithm

**Search State Definition.** Let the input atomic sequence be denoted by  $C_{\text{atoms}} = [A, A, A, \dots, B, B, B, B, B, \dots, C, C, \dots]$ , as defined in the main text. We define  $\mathcal{E} = \{A, B, C, \dots\}$  as the set of unique element types present in  $C_{\text{atoms}}$ . A hypothesis at step  $n$  is formally defined as a tuple  $h_n = (\mathbf{l}_{1:n}, s_{1:n}, \mathbf{Count}_{1:n})$ , where:

- $\mathbf{l}_{1:n} = [l_1, \dots, l_n]$  is the partial sequence of assigned Wyckoff letters up to atom  $n$ .
- $s_{1:n} = \sum_{i=1}^n \log p_w(l_i | C_{\text{atoms}})$  is the cumulative log-probability score of the assignment sequence.
- $\mathbf{Count}_{1:n} \in \mathbb{N}^{|\mathcal{E}| \times |L(S_g)|}$  is the global counter matrix. The entry  $\mathbf{Count}_{1:n}[e, l]$  records the number of atoms of element type  $e \in \mathcal{E}$  that have been assigned to Wyckoff letter  $l$  within the partial sequence  $\mathbf{l}_{1:n}$ . This matrix allows for the independent verification of multiplicity constraints for each element type.

**Expansion and Pruning.** At step  $n$ , let the current atom be  $e_n = C_{\text{atoms}}[n]$ . We consider assigning a letter  $l \in L(S_g)$ . To accelerate the search, candidate letters are evaluated in descending order of their probability  $p_w(l_n = l | C_{\text{atoms}})$ . We enforce the algebraic consistency constraint via an *early pruning* check: a branch is valid if and only if the current count  $\mathbf{Count}_{1:n}[e_n, l]$  plus the number of remaining atoms of element  $e_n$  in the sequence is sufficient to reach the next integer multiple of  $\text{mult}(l)$ . Branches failing this check are discarded immediately.

The complete procedure is detailed in Algorithm 1.

### A.4. Diffusion Rectification via Predicted Symmetry

Once the optimal space group  $S_g$  and the atom-wise Wyckoff assignment  $\mathbf{l}^* = \{l_1^*, \dots, l_N^*\}$  are determined,

we utilize them to rectify the intermediate states of the diffusion process. This rectification is applied at each denoising step  $t$  to explicitly enforce symmetry constraints on the lattice and fractional coordinates.

**Lattice Rectification.** The lattice matrix  $\mathbf{L}_t$  is parameterized by a coefficient vector  $\mathbf{k}_t \in \mathbb{R}^6$  in the  $O(3)$ -invariant logarithmic space [10]. The inferred space group  $S_g$  imposes hard constraints on specific dimensions of  $\mathbf{k}_t$ . By enforcing these constraints, we ensure that the resulting lattice vectors strictly adhere to the specific edge lengths and angular relationships mandated by the crystal system. Let  $\mathbf{m}_{S_g} \in \{0, 1\}^6$  be the binary mask where 0 indicates a constrained dimension. We rectify the lattice state via:

$$\hat{\mathbf{k}}_t = \mathbf{m}_{S_g} \odot \mathbf{k}_t + (1 - \mathbf{m}_{S_g}) \odot \mathbf{k}_{ideal}, \quad (\text{A11})$$

where  $\mathbf{k}_{ideal}$  represents the exact theoretical values required by the crystal family of  $S_g$  (e.g., ensuring  $90^\circ$  angles or equal edge lengths).

**Coordinate Rectification via Subspace Projection.** In the absence of hard constraints, the fractional coordinates  $\mathbf{F}_t \in \mathbb{R}^{N \times 3}$  generated at step  $t$  inevitably violate the strict site symmetries derived in Step 2. We employ a *Project-and-Reconstruct* mechanism to rectify  $\mathbf{F}_t$  into a symmetry-compliant state  $\hat{\mathbf{F}}_t$ .

For each Wyckoff orbit  $w$  identified in  $\mathbf{l}^*$ , let  $\mathcal{I}_w$  be the set of atom indices belonging to this orbit. The positions of these atoms are geometrically related via affine transformations  $\{(\mathbf{R}_n, \mathbf{t}_n)\}_{n \in \mathcal{I}_w}$ . We perform the rectification in two substeps:

First, we aggregate the fractional coordinates  $\mathbf{F}_t$  at the current denoising step  $t$  to estimate a robust canonical base coordinate  $\mathbf{F}'_t$  (representing the generator of the orbit). This is formulated as a least-squares problem minimizing the deviation from symmetry operations. The optimal solution is computed via the Moore-Penrose pseudoinverse:

$$\mathbf{F}'_t = \frac{1}{|\mathcal{I}_w|} \sum_{n \in \mathcal{I}_w} \mathbf{J}_w^\dagger (\mathbf{f}_{t,n} - \mathbf{t}_n), \quad (\text{A12})$$

where  $\mathbf{f}_{t,n}$  is the  $n$ -th row of  $\mathbf{F}_t$ , and  $\mathbf{J}_w^\dagger$  is the pseudoinverse of the site-symmetry Jacobian matrix, projecting the coordinates onto the valid degrees of freedom (e.g., a specific axis or plane) defined by the Wyckoff letter.

Second, we strictly reconstruct the symmetry-compliant state  $\hat{\mathbf{F}}_t$  by broadcasting the canonical base coordinate  $\mathbf{F}'_t$  back to all equivalent atoms in the orbit. For each  $n \in \mathcal{I}_w$ , the rectified coordinate  $\hat{\mathbf{f}}_{t,n}$  (the  $n$ -th row of  $\hat{\mathbf{F}}_t$ ) is explicitly computed as:

$$\hat{\mathbf{f}}_{t,n} = \mathbf{R}_n \mathbf{F}'_t + \mathbf{t}_n. \quad (\text{A13})$$

By simultaneously replacing the noisy states  $\mathbf{k}_t$  and  $\mathbf{F}_t$  with their rectified counterparts  $\hat{\mathbf{k}}_t$  and  $\hat{\mathbf{F}}_t$  at the end

---

**Algorithm 1:** Constrained Beam Search with Matrix-based State Tracking

---

**Input:** Probability distribution  $p_w$  (from Eq. 2), Space group  $S_g$ , Atomic sequence  $C_{\text{atoms}} = [A, \dots, B, \dots]$ , Unique elements  $\mathcal{E}$ .

**Output:** Optimal assignment sequence  $\mathbf{l}^*$ .

// --- Phase 1: Initialization ---

1 Set Beam Width  $K$ ,  $L_{\text{valid}} \leftarrow L(S_g)$   
 // Initialize state at step 0: empty list, zero score, zero matrix

2  $\mathcal{B}_0 \leftarrow \{(\emptyset, 0, \mathbf{0}_{|\mathcal{E}| \times |L_{\text{valid}}|})\}$ ,  $\mathbf{l}^* \leftarrow \text{None}$ ,  $s^* \leftarrow -\infty$

// --- Phase 2: Iterative Search ---

3 for  $n \leftarrow 1$  to  $N$  do

4    $\mathcal{B}_n \leftarrow \emptyset$

5    $e_n \leftarrow C_{\text{atoms}}[n]$  ▷ Element type of the  $n$ -th atom

6    $N_{\text{rem}} \leftarrow |\{k \mid n < k \leq N, C_{\text{atoms}}[k] = e_n\}|$

7   // Sort candidates by conditional probability for the  $n$ -th atom  
 $\mathcal{L}_{\text{sorted}} \leftarrow \text{Sort}(L_{\text{valid}}) \text{ by } p_w(l_n = l \mid C_{\text{atoms}}) \text{ descending}$

8   for each hypothesis  $(\mathbf{l}_{1:n-1}, s_{1:n-1}, \mathbf{Count}_{1:n-1}) \in \mathcal{B}_{n-1}$  do

9     for each letter  $l \in \mathcal{L}_{\text{sorted}}$  do

10       // Update cumulative log-probability  
 $s_{1:n} \leftarrow s_{1:n-1} + \log p_w(l_n = l \mid C_{\text{atoms}})$   
 $// \text{Update counter matrix for step } n$

11        $\mathbf{Count}_{1:n} \leftarrow \text{Copy}(\mathbf{Count}_{1:n-1})$   
 $\mathbf{Count}_{1:n}[e_n, l] \leftarrow \mathbf{Count}_{1:n}[e_n, l] + 1$   
 $// \text{Pruning: Check algebraic consistency}$

12        $c \leftarrow \mathbf{Count}_{1:n}[e_n, l]$   
 $m_{\text{req}} \leftarrow \lceil \frac{c}{\text{mult}(l)} \rceil \times \text{mult}(l)$

13       if  $c + N_{\text{rem}} \geq m_{\text{req}}$  then  
 $\quad \quad \quad \text{Add } (\mathbf{l}_{1:n-1}.\text{append}(l), s_{1:n}, \mathbf{Count}_{1:n}) \text{ to } \mathcal{B}_n$

14     

15     

16     

17   // Keep best  $K$  by score  $s_{1:n}$   
 $\mathcal{B}_n \leftarrow \text{TopK}(\mathcal{B}_n, K)$

// --- Phase 3: Final Selection ---

18 for each  $(\mathbf{l}, s, \mathbf{Count}) \in \mathcal{B}_N$  do

19   // Final Validation: All counts must be exact multiples  
 $is\_valid \leftarrow \forall e \in \mathcal{E}, l \in L_{\text{valid}} : \mathbf{Count}[e, l] \bmod \text{mult}(l) = 0$

20   if  $is\_valid$  and  $s > s^*$  then  
 $\quad \quad \quad \mathbf{l}^* \leftarrow \mathbf{l}$ ,  $s^* \leftarrow s$

21   

22 return  $\mathbf{l}^*$

---

of each denoising step, we ensure that both the atomic configuration and the unit cell geometry strictly evolve on the geometric manifold defined by the target Wyckoff symmetries.

## Appendix B: Hyper-parameters and Training/Inference Configurations

Complementing the mathematical formulations and algorithmic designs detailed in Supplementary Information A, which define the structural logic of our method, this part provides the granular implementation specifications necessary for reproducibility. We herein explicitly list the concrete hyperparameter valuations, optimization protocols, and inference settings used in our experiments. These configurations instantiate the abstract models into the specific computational pipelines employed to yield

the reported results. Please note that the specifications listed in this section exclusively pertain to our proposed symmetry prediction method. Regarding the generative diffusion backbone, we strictly adhere to the original configurations of DiffCSP++ [10]. We utilized its official open-source implementation with identical hyperparameters, training schedules, and inference protocols, with the sole intervention being the substitution of the CSPML-retrieved templates with our *ab initio* predicted templates.

### B.1. Data Representations and Tensor Shapes

To clarify the data flow described in the methodology, we formally define the shapes of the input and output tensors used in our implementation. The batch size  $B$  is set as 32. We set the maximum sequence length  $L = 128$

and maximum multiplicity slots  $M = 30$ .

- **Inputs:** The atomic sequence input is represented as  $\mathbf{x} \in \mathbb{N}^{B \times L}$ , with an associated padding mask  $\mathbf{m} \in \{0, 1\}^{B \times L}$ . The conditioning space group labels are denoted as  $\mathbf{s} \in \mathbb{N}^B$ . For multiplicity constraints, we utilize a multiplicity sequence  $\mathbf{u} \in \mathbb{N}^{B \times M}$  with a mask  $\mathbf{m}_u \in \{0, 1\}^{B \times M}$ .
- **Embeddings:** The output of the token embedding layer (Eq. 4 in Appendix A) corresponds to a tensor  $\mathbf{E}(\mathbf{x}) \in \mathbb{R}^{B \times L \times D}$ , where  $D = 256$  is the hidden dimension.
- **Outputs:** The model produces unnormalized logits  $\mathbf{O} \in \mathbb{R}^{B \times L \times C}$ , where  $C = 25$  is the size of the Wyckoff letter vocabulary. These logits form the basis for the probability distribution  $p_w$  used in the beam search.

## B.2. Model Architecture and MoE Settings

We employ a BERT-style Transformer encoder enhanced with Soft Mixture-of-Experts (SoftMoE) layers. The specific architectural hyperparameters are summarized in Table III. Consistent with the notation in Appendix A,  $D$  denotes the hidden embedding dimension, and  $H$  represents the number of attention heads.

## B.3. Training and Testing Settings

The optimization protocols for training and the inference configurations for testing are unified in Table IV. We utilize the AdamW optimizer with a cosine annealing scheduler for training, and a constrained beam search with a fixed beam width for testing.

## Appendix C: Evaluation Metrics and Benchmark Datasets

### C.1. Evaluation Metrics: The SUN and Matching Rate Metrics

Following the protocol defined by Zeni et al. [14], we evaluate generative quality using the SUN metrics. Leveraging the low inference cost of our model, we adopt a *Top-20* evaluation strategy: for each test composition, we generate 20 candidate structures. Each candidate is assessed against three criteria:

- **Stability.** A structure is classified as *stable* if its formation energy is within 0.1 eV/atom of the convex hull of competing phases. To ensure computational feasibility for large-scale generation, we follow Zeni et al. [14] and utilize MatterSim [29], a

machine learning force field trained on extensive DFT trajectories, for geometry optimization and energy evaluation.

- **Uniqueness.** A structure is considered *unique* if it is not structurally equivalent to any other sample within the generated batch of 20 candidates. Equivalence is determined using the robust structure matcher from Zeni et al. [14], which extends `pymatgen`'s `StructureMatcher` [30] to handle partial occupancies, elemental substitutions, and symmetry tolerances.
- **Novelty.** A structure is labeled *novel* if it is not structurally equivalent to any entry in the combined reference database. We construct this reference set by merging the Alexandria and MP-20 datasets [26, 31], yielding a comprehensive collection of 845,997 materials. The matching process permits up to a 10% deviation in elemental ratios to account for stoichiometric variability.

Accordingly, the Top-20 SUN score represents the success rate at the composition level. A composition is considered solved if at least one of its 20 candidates simultaneously satisfies the stability, uniqueness, and novelty criteria:

$$\text{Top-20 SUN} = \frac{N_{\text{stable} \cap \text{unique} \cap \text{novel}} @ \text{Top-20}}{N_{\text{total}}} \times 100\%, \quad (\text{C1})$$

where  $N_{\text{stable} \cap \text{unique} \cap \text{novel}}$  is the number of test compositions that yielded at least one valid candidate satisfying all three conditions, and  $N_{\text{total}}$  is the total number of compositions in the test set.

Complementary to the SUN protocol, we employ the **Matching Rate** to evaluate the model's ability to recover specific ground-truth (GT) structures. For each composition in the test set, we generate  $k = 20$  samples and identify a successful match if at least one sample is structurally equivalent to the corresponding GT structure. This structural equivalence is determined using the `StructureMatcher` class in `pymatgen` with a rigorous set of thresholds: fractional length tolerance  $\text{stol} = 0.5$ , angle tolerance  $\text{angle_tol} = 10^\circ$ , and lattice vector tolerance  $\text{ltol} = 0.3$ .

Accordingly, the Top-20 Matching Rate is defined as the proportion of matched compositions over the entire test set:

$$\text{Top-20 Matching Rate} = \frac{N_{\text{matched}} @ \text{Top-20}}{N_{\text{total}}} \times 100\%. \quad (\text{C2})$$

The complementarity of Top-20 SUN and Top-20 Matching Rate lies in their distinct evaluative focuses: the SUN metric emphasizes discovery and viability, rewarding the model's capability to explore unknown chemical spaces and generate physically plausible materials

that do not necessarily exist in the training distribution. Conversely, the Matching Rate measures reconstruction fidelity, quantifying how accurately the model can capture the underlying distribution of known experimental or high-quality DFT structures. Together, they provide a holistic reflection of the generative model’s performance, balancing the requirement for creative exploration with the necessity of structural accuracy.

## C.2. Benchmark Datasets

To ensure a fair comparison with the baseline method DiffCSP++ [10], we utilize the same three benchmark datasets with identical training, validation, and test splits.

- **Perov-5** [25]: A dataset containing 18,928 perovskite-type structures. Each unit cell contains exactly 5 atoms. This dataset provides a controlled environment for evaluating compositional generalization under a fixed topological constraint.
- **MP-20** [26]: Comprising 45,231 experimentally verified materials from the Materials Project, this dataset includes diverse crystal systems with up to 20 atoms per conventional unit cell. It serves as a balanced benchmark for structural and compositional diversity.
- **MPTS-52** [10]: A more challenging dataset consisting of 40,476 structures with up to 52 atoms per unit cell. It represents a broader sampling of the complex real-world crystal structure space, testing the model’s scalability to larger systems.

TABLE III: Hyperparameter settings for the model architecture and SoftMoE layers.

Category	Parameter	Value
<b>Transformer Backbone</b>	Layers ( $L_{depth}$ )	6
	Hidden Dimension ( $D$ )	256
	Attention Heads ( $H$ )	8
	Head Dimension ( $d_h$ )	32
	FFN Hidden Dimension	512
<b>SoftMoE</b>	Dropout Rate	0.15
	MoE Layers	All 6 layers
	Total Experts ( $E$ )	8
	Active Experts ( $k$ )	2 (Top- $k$ Router)
	Capacity Factor	1.5
	Router Noise Std	0.5
<b>Vocabulary Sizes</b>	Aux Loss Coefficient	0.002
	Element Tokens	90 (include <pad>, <unk>)
	Space Group Tokens ( $S_g$ )	169 (include <unk>)
	Wyckoff Labels ( $C$ )	25 (include <pad>)

TABLE IV: Combined settings for optimization, training loop, and testing inference.

Category	Hyperparameter	Value
<b>Optimization</b>	Optimizer	AdamW
	Learning Rate (LR)	$1 \times 10^{-4}$
	Weight Decay	0.01
	Betas	(0.9, 0.98)
	Epsilon	$1 \times 10^{-8}$
	Gradient Clipping	1.0
<b>Scheduling</b>	Scheduler	ReduceLROnPlateau (monitor: <code>val_loss</code> )
	Factor / Patience	0.5 / 3
	Threshold	$5 \times 10^{-4}$
	Min LR	$1 \times 10^{-6}$
<b>Training Loop</b>	Max Epochs	200
	Batch Size	32
	Gradient Accumulation	4 steps
	AMP (Mixed Precision)	Enabled
	Early Stopping Patience	10 epochs
<b>Testing &amp; Inference</b>	Beam Width (K)	100
	Search Strategy	Constrained Beam Search
	Sorting Criterion	Log-likelihood (descending)